



Effect of System Dynamics on Surface Topography in Fast Tool Servo-Based Diamond Turning of Microlens Arrays

Takeshi Hashimoto¹ · Jiwang Yan²

Received: 29 December 2024 / Revised: 14 March 2025 / Accepted: 15 March 2025
© The Author(s) 2025

Abstract

A lens array is often used for optical components of sensing devices, requiring high surface quality and form accuracy. Fast tool servo (FTS)-based diamond turning is one of the technologies for manufacturing complicated shapes, such as freeform optics, structured surfaces, and microlens arrays, with high machining efficiency. In this study, lens array machining was performed on copper using an FTS on a diamond turning machine. For evaluating the lens array surface topography, the focus was on surface waviness formation. As a dominating factor of surface waviness, the system dynamics behavior was investigated by capturing and analyzing the position signal. It was found that a specific waviness pattern could be formed on the surface due to the servo response. By considering the dynamics of the FTS system from the captured signals, the FTS system behavior was identified, and optimal machining parameters for the lens array were proposed. A machining test under the optimized cutting conditions reduced the average Sdq used to quantify the waviness amount from 93 to 50 μrad and the standard deviation from 33 to 3 μrad , which greatly improved the consistency in accuracy for all lens arrays. This study will contribute to the appropriate utilization of FTS systems in the ultraprecision machining of various advanced optics, such as microlens arrays.

Highlights

1. Surface waviness formation in diamond turning of lens arrays with a fast tool servo was investigated.
2. A specific waviness pattern was identified, which was dominated by the dynamics of the tool servo system.
3. Uniform form accuracy was achieved by optimizing the machining conditions based on the system dynamics.

Keywords Diamond turning · Fast tool servo · Lens array · Surface quality · Surface waviness

1 Introduction

With recent rapid technological advancements, optical technology has emerged as a cornerstone of innovation across multiple industries. Applications that require precision,

such as high-resolution imaging for consumer electronics and telescope optics [1, 2], ophthalmic devices for myopia control [3, 4], AR/VR wearable devices [5, 6], and sensing systems for autonomous technologies [7, 8], highlight the growing importance of advanced optical components. Among these, the fabrication of lens arrays has attracted considerable attention owing to its pivotal role in advancing optical technologies. One notable application of lens arrays is in Shack–Hartmann wavefront sensors (SHWSs), which were originally developed to address atmospheric aberrations in satellite imaging. The integration of lens arrays allows SHWSs to measure wavefront errors with unprecedented accuracy, thereby transforming the field of optical metrology [9, 10]. Beyond wavefront sensing, lens arrays are

✉ Jiwang Yan
yan@mech.keio.ac.jp

¹ School of Integrated Design Engineering, Graduate School of Science and Technology, Keio University, Yokohama 223-8522, Japan

² Department of Mechanical Engineering, Faculty of Science and Technology, Keio University, Yokohama 223-8522, Japan

vital in laser beam homogenization, transforming irregular intensity distributions into uniform “top hat” profiles. Innovations such as chirped microlens arrays have enhanced performance by mitigating interference patterns and improving intensity homogeneity [11, 12]. In addition, the lens array design is used in ophthalmic medical devices such as myopia control glasses for children. The lens array patterns on the spectacle lens design are one of the solutions to slow the progression of myopia. [4, 13, 14].

Ultraprecision diamond machining is widely used for fabricating optical components with high surface quality and form accuracy. Micromilling and fly-cutting processes are versatile for fabricating complex optical surfaces [15–17]. However, one of the challenges is processing speed, which is one of the bottlenecks to efficiency and limits productivity [18]. Ultraprecision diamond turning has long been a fundamental process in the fabrication of rotationally symmetric surfaces, offering nanometer-level form accuracy and remarkable surface quality. Among these advancements, fast tool servo (FTS)-based diamond turning technology is a manufacturing technique that can fabricate complicated shapes with high productivity, such as freeform optics, structured surfaces, and microlens arrays, compared to conventional methods such as slow tool servo (STS)-based diamond turning, which uses the X-, Z-, and C-axes simultaneously, and micromilling processes [19, 20]. Extensive research has been conducted regarding FTS systems utilized in optical manufacturing. To et al. [21] demonstrated lens array fabrication using a piezoelectrically driven FTS system on a diamond turning machine and investigated the surface roughness and form accuracy by optimizing the cutting conditions. Tanikawa et al. [22] demonstrated the manufacturing of a random dimple array for an optical diffuser by an independent voice coil-driven FTS and proposed a process to generate a sharp edge at the boundary of the arrays. Huang et al. [23] considered the relationship between the effect of the dynamics of the servo system and form error and proposed to control the form accuracy on microlens array machining utilizing STS and FTS together. Zhang et al. [24] introduced an optimization method for FTS-based diamond turning, utilizing an adaptive control sampling point strategy to optimize the tool trajectory and minimize interpolation errors, and demonstrated the fabrication of intricate surfaces with improved form accuracy. However, the literature specifically addressing the surface topography of complex surfaces fabricated using FTS-based diamond turning remains limited. In particular, there is no in-depth analysis of the relationship between the system’s dynamic behavior and surface waviness.

In this study, lens array fabrication was demonstrated using an FTS system on an ultraprecision diamond turning machine, and the surface topography of the lens array was investigated to understand its relationship with cutting

Table 1 Lens array design information

Item	Value
Workpiece material	Oxygen-free copper
Workpiece dimension (mm)	50
Diameter of the lenslet (mm)	1.7
Radius of the lenslet (mm)	20 (Concave)
Lens edge slope (°)	2.15
Lens SAG (μm)	18
Layout of the lens array	10 \times 10
Lens pitch (mm)	3.5 (X), 3.5 (Y)
Total number of lenses	100

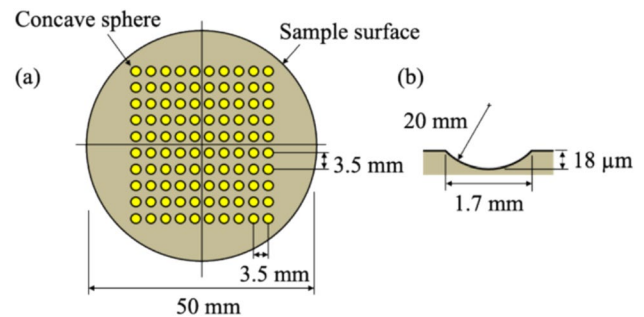


Fig. 1 a Lens array design layout; b lens shape design in detail

parameters. Particularly, the surface waviness formation due to the servo dynamics behavior was investigated by analyzing the position signal from the FTS system and comparing it with the surface topography. Consequently, an appropriate cutting strategy for lens array machining using an FTS was proposed and demonstrated to be effective in reducing surface waviness.

2 Experimental Method

2.1 Lens Array Design

The lens array was designed by targeting an imaging device application that is highly sensitive to the surface topography, especially its surface waviness [25]. Conversely, for demonstration purposes, to verify the surface topography more precisely by utilizing the optical profilometer, the design should be within the metrology range, especially the slope limitation, to measure without any measurement error from the instrument. Based on these considerations, the lens array design for this study was selected, as shown in Table 1. The layout of a 10 \times 10 lens array and the lens shape design are shown in Fig. 1a, b, respectively. Using this design, a coherence scanning interferometric (CSI) optical profilometer with appropriate lens selection can individually evaluate

each machined lens surface with high-resolution map data. Oxygen-free copper was selected as the workpiece material because it has less influence on tool wear-induced form error than other materials, such as steel and nickel plating.

2.2 Experimental Setup

An ultraprecision diamond turning machine, Nanoform X (AMETEK Precitech Inc., USA), with XYZBC five-axis simultaneous control, was used as the machining platform for this testing. The ultraprecision machine has an air-bearing work spindle, oil hydrostatic linear slides, and a rotary table with full closed feedback control to enable nanometric feedback resolution. It also utilizes an FTS system (FTS5000, AMETEK Precitech Inc., USA) as an additional axis (W-axis) that allows synchronized position control based on X- and C-axis encoder information. It has an air-bearing piston with a 5 mm full stroke, and its position control uses a fully closed feedback system with a glass scale. A voice coil motor drive is used for rapid tool motion. A photograph of the machine setup is shown in Fig. 2. The block diagram of the FTS system is shown in

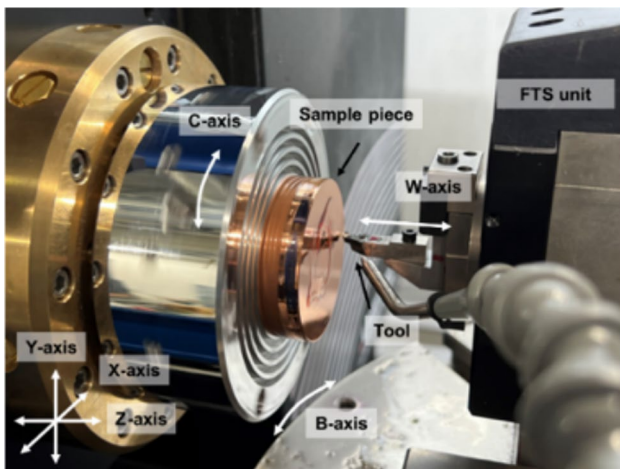


Fig. 2 Machine setup for FTS lens array fabrication

Fig. 3. This independent FTS system can acquire data to capture the command signal and the actual position signal from the controller. Data acquisition can be executed while the program runs at a sampling frequency of 20 kHz. To evaluate the machined surface, a CSI optical profilometer (Nexview NX2, Zygo Corporation., USA) was used to measure the surface topography. An objective lens with 10 times magnification was used for the evaluation, which has a 1.8 mm × 1.8 mm field of view with 1.8 μm pixel resolution.

2.3 Cutting Parameters

The FTS velocity and acceleration circumstances should be considered during machining to determine the cutting parameters for this lens array because the FTS has an acceleration hardware limitation with continuous acceleration of 25 G [26]. Therefore, the cutting parameters must be determined within a limited range. Using the design information, a maximum acceleration of 25 G was hit at a spindle speed of 150 rpm. Based on this restriction, the cutting parameters listed in Table 2 were used in this study. From the initial calculation of its acceleration, the maximum acceleration at 125 rpm was 22 G, within the FTS acceleration limit of 25 G.

Table 2 Cutting parameters

Item	Value
Tool	Natural diamond tool
Tool radius (mm)	0.496
Tool rake angle (°)	0
Tool clearance angle (°)	13
Spindle speed (rpm)	125
Spindle rotation direction	Clockwise
Finish feed rate (mm/rev)	0.002
Finish depth of the cut (mm)	0.002
Coolant	Oil mist

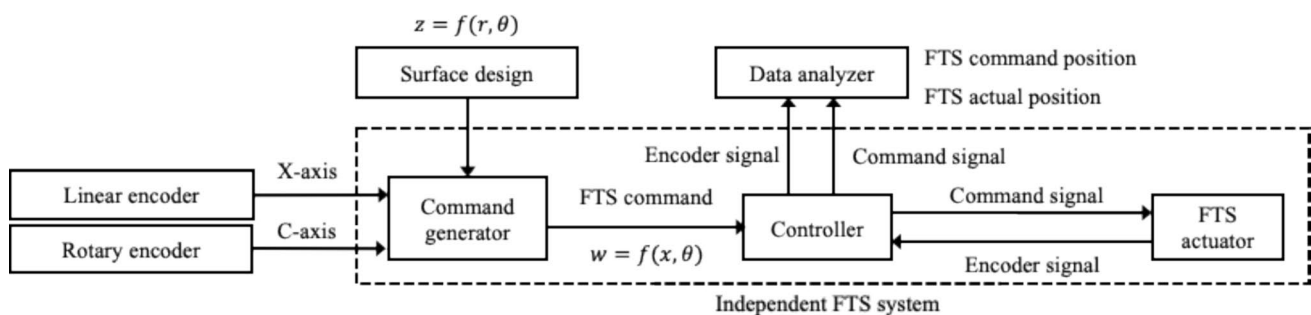


Fig. 3 Diagram of the signal flow for the FTS system

3 Results and Discussion

3.1 Machined Surface Topography

A photograph of the fabricated lens array on the workpiece under the above cutting conditions is shown in Fig. 4a. Three locations for measurement were selected from the machined lens array: edge, halfway, and close to the center, as shown in Fig. 4b. The surface topography measurement results at these locations are shown in Fig. 5a–c, respectively. Regarding the evaluation process, a form removal process with a fourth-order polynomial was applied to the measurement data to remove the form from the raw measurement data. After the form removal process, a low-pass Gaussian filter with a wavelength of $100\ \mu\text{m}$ was used to smooth the data to eliminate noise and spikes in the measurement results. To describe the surface topography, the surface roughness parameter S_q (root mean square of the height distribution) was selected. The results of the surface roughness measurements are shown in Fig. 5. The surface roughness values at locations (1,1), (3,3), and (5,5) were 4.9, 2.1, and 1.8 nm, respectively. The closer the location is to the rotational center, the lower the surface roughness. By examining the surface topography, Fig. 5a reveals a distinct waviness pattern across the entire surface. Figure 5b displays a slight waviness pattern in the right corner, while Fig. 5c exhibits no apparent pattern.

Figure 6 presents the surface topographies of the corner lenslets. The measured lenslet locations are shown in Fig. 6a. Figure 6b–d, and (e) correspond to locations (1,1), (1,10), (10,1), and (10,10), respectively. At these locations, the distance from the rotational center to each meridian of the arrays was identical at $22.7\ \text{mm}$. Consequently, the surface speed was at $17\ \text{m/min}$ with a spindle speed of $125\ \text{rpm}$. A similar waviness pattern was observed across all locations. Regarding the orientation of the waviness pattern, the highest waviness positions aligned with the tool trajectory directions. According to the cutting parameters in Table 2, the spindle rotated clockwise, indicating that the highest

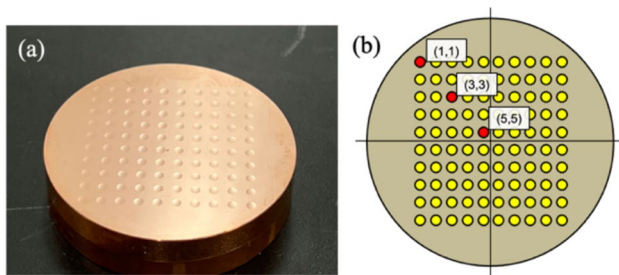


Fig. 4 a Picture of the machined sample; b surface measurement locations

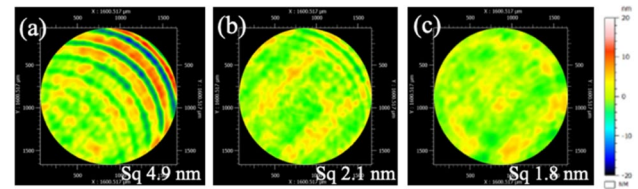


Fig. 5 Surface roughness and profile: a location (1,1), b location (3,3), and c location (5,5)

waviness positions correspond to the locations where the tool initially engaged with the surface. In terms of surface roughness, the measured S_q values were 4.9, 4.7, 4.7, and 4.4 nm at locations (1,1), (10,1), (1,10), and (10,10), respectively, with a standard deviation of 0.2 nm, confirming that the surface roughness values were similar. Based on the standard deviation assessment of the surface roughness, the repeatability of the machining process in this study was considered high.

In addition, to evaluate the repeatability of the process in this study, three samples were machined using the same cutting parameters shown in Table 2. Figure 7 shows the measurement results of the surface topography at location (1,1).

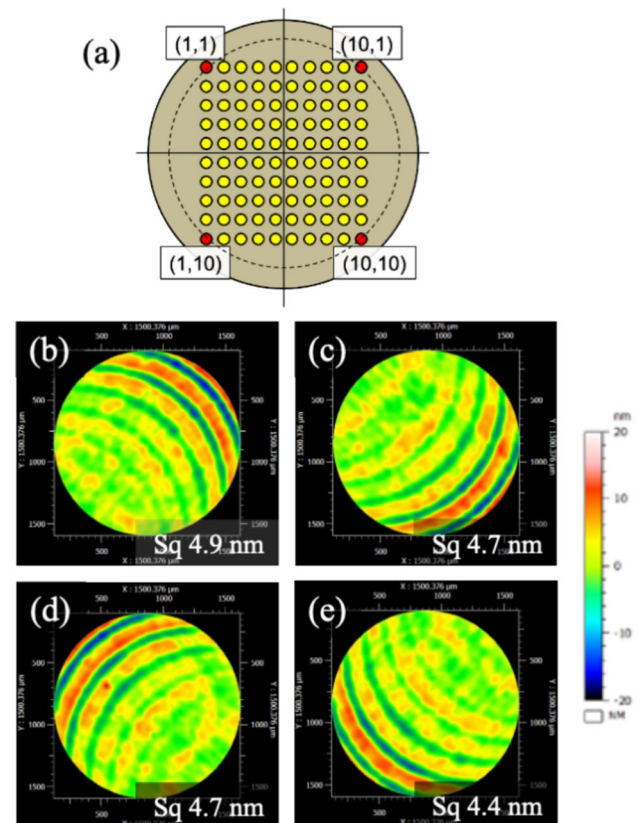


Fig. 6 Surface roughness evaluation at the corner lenslets: a measured lenslet locations; surface roughness b at (1,1), c at (10,1), d at (1,10), and e at (10,10)

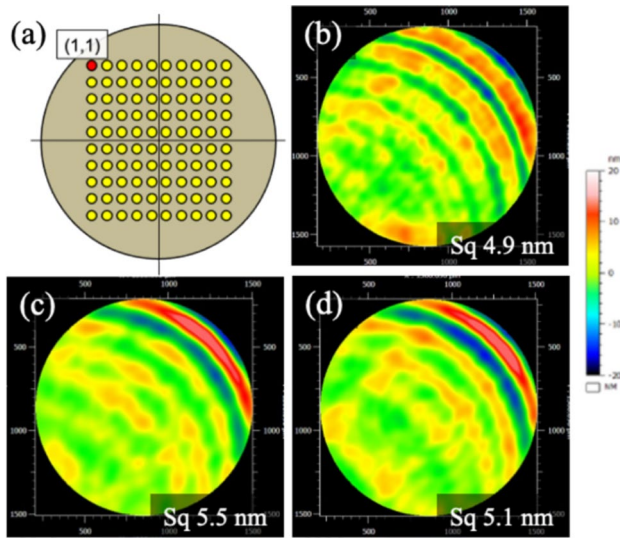


Fig. 7 Repeatability of the surface topography at location (1,1) across multiple samples: **a** measured lenslet location; surface roughness of **b** sample #1, **c** sample #2, and **d** sample #3

The surface roughness (Sq) values were 4.9, 5.5, and 5.1 nm for sample #1, sample #2, and sample #3, respectively. The standard deviation of these three results was 0.3 nm, which indicates that the repeatability of this machining is also considered enough.

3.2 Waviness Evaluation

There are several approaches to visualizing and quantifying surface waviness. In particular, Sdq is the root mean square of the gradient, following ISO25178-2 for surface parameters [27], which can describe the slope change on the surface quantitatively and is strongly related to surface waviness. The mathematical description is shown in Eq. (1). For optical applications, a fast slope change on the surface considerably degrades the optical performance, especially in imaging optics [25]. Therefore, to evaluate the waviness amount, this parameter was selected to investigate the waviness appearance owing to the machining parameters used in this study.

$$Sdq = \sqrt{\frac{1}{A} \iint_A \left[\left(\frac{\partial(x,y)}{\partial x} \right)^2 + \left(\frac{\partial(x,y)}{\partial y} \right)^2 \right] dx dy} \quad (1)$$

The result of this analysis for sample #1 is shown in Fig. 8. Figure 8a shows the lenslet numbering corresponding to the distribution map shown in Fig. 8b. The Sdq distribution map result for all 10×10 lenslets shows a noticeable trend in the outer lenslets with large Sdq values. At the near center area, the minimum Sdq value was 45 μrad; in contrast, at the edge, the maximum value was 182 μrad, four

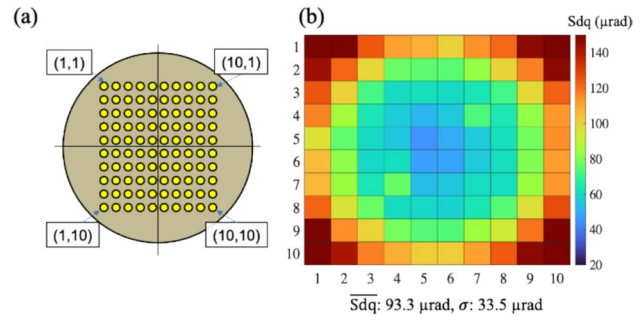


Fig. 8 Waviness evaluation result using Sdq: **a** schematic of the lenslet locations; **b** result of the waviness distribution for all lenslets

Table 3 Reproducibility of the repeated machining test

Sample number	\overline{Sdq} (μrad)
#1	93.3
#2	95.3
#3	82.9
Average	90.5
Standard deviation	6.7

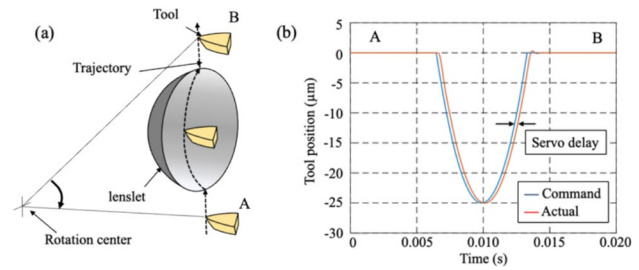


Fig. 9 **a** Schematic of the tool motion on the lenslet by FTS; **b** trajectories of the command and actual profiles captured from the system

times larger than the center area. The average Sdq value was 93.3 μrad, and the standard deviation of Sdq was 33.5 μrad. According to this result, the larger the distance from the rotational center, the larger the surface waviness. In this experiment, the rotational speed was maintained at 125 rpm. Therefore, the surface speed was high toward the edge, and the FTS had to respond fast. The surface speed at the corner lenslet was 17 m/min. Table 3 shows the repeatability results from three repeated samples. The standard deviation of these samples was analyzed, indicating that the process repeatability, represented by the standard deviation in this study, was 6.7 μrad for the average Sdq value.

3.3 FTS Position Signal Analysis

The captured signals are shown in Fig. 9. The command and encoder signals were split inside the controller to output and

captured by the data analyzer, as shown in Fig. 3. This plot consists of the command and actual tool positions. However, it contains the servo delay error. Therefore, to analyze the tool position error directly related to the surface topography, the servo delay amount was calculated from the captured signals and canceled out as the servo delay by 223.5 μ s.

The results of the position error analysis after removing the servo delay are shown in Fig. 10. These plots were obtained by running the program at the meridian of the lens shape, with surface speeds of (a) 20 m/min, (b) 15 m/min, (c) 10 m/min, and (d) 5 m/min. The two spikes on the left and right are where the tool moves in and out. The area between these spikes corresponded to the machined area. According to the analysis, it is evident that the profile has a ripple pattern at 20 m/min surface speed. The more the surface speed decreases, the less the waviness that appears. Figure 11 shows a comparison between the following error plot and the waviness profile of the surface. The cycle of the ripple pattern on the following error plot at 20 m/min surface speed was 0.75 ms.

In contrast, the waviness cycle on the surface profile at the corner lenslet was observed at 0.205 mm. To understand the relationship between the ripple cycle in the following error and the waviness cycle on the surface, the waviness cycle time was calculated by converting it to surface speed. The calculation result was obtained at 0.70 ms, which almost agrees with the observed ripple cycle in the following error plot. According to this observation result, the FTS motion at the edge of the tool trajectory commands an immediate direction change, and the FTS system vibrates and damps, as in the step response curve behavior of the high-order control system. The results obtained in this experiment also show that the resonance frequency can be estimated to be between 1333 and 1428 Hz from the analyzed ripple cycles of 0.70 and 0.75 ms, respectively.

Figure 12 shows a comparison of the settling time with different surface speeds. The signal noise level was observed

to determine the settling time based on the obtained results. The noise level was calculated using the position signal when the system remained stationary. To determine the settling time from the signal, the threshold level was used as the average amplitude of the sitting still profile, and it was set at 5 nm (± 2.5 nm) as the settling range, which was 95% of the profile amplitude of the noise level in this study. Using the threshold setup, the settling time results of this system were between 1.3 and 4.0 ms.

3.4 System Dynamics Analysis

As shown by the servo position data analysis described in Sect. 3.3, the servo motion considerably affected the surface waviness. By clarifying the relationship between the FTS

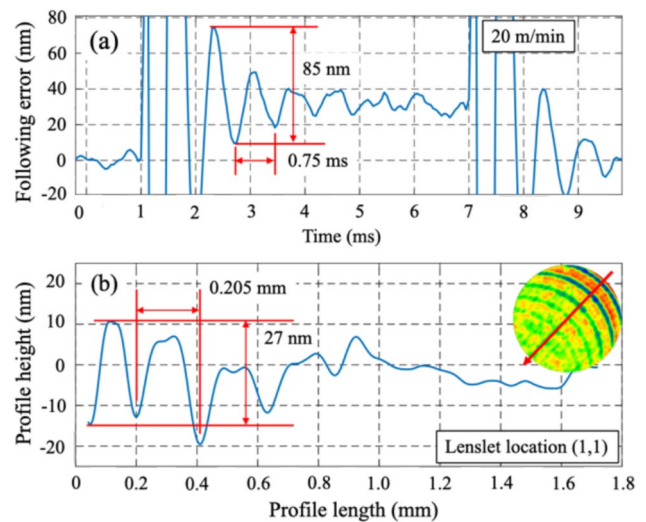


Fig. 11 a Following error plot for the 20 m/min surface speed; b surface profile of the corner lenslet

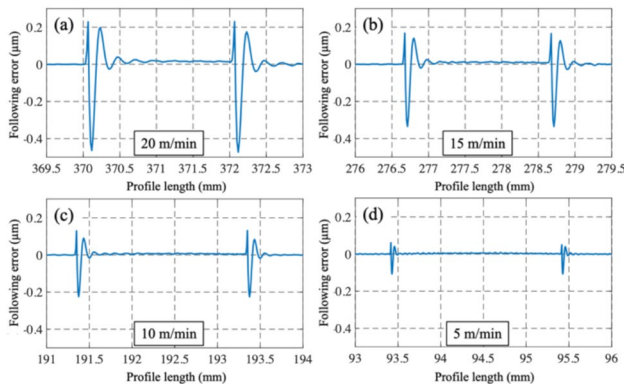


Fig. 10 Comparison of the following error plots with different surface speeds: a 20 m/min, b 15 m/min, c 10 m/min, and d 5 m/min

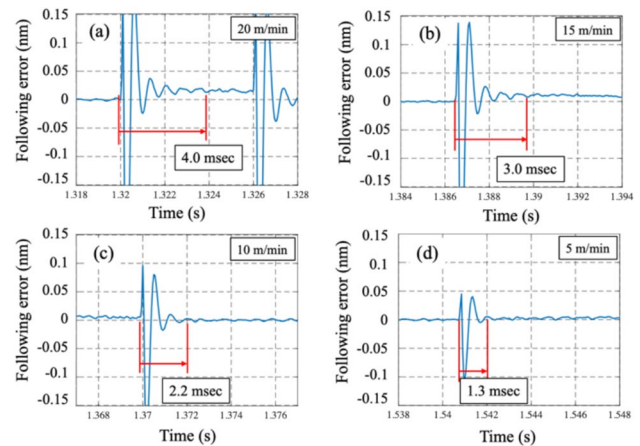


Fig. 12 Comparison of the settling time with different surface speeds: a 20 m/min, b 15 m/min, c 10 m/min, and d 5 m/min

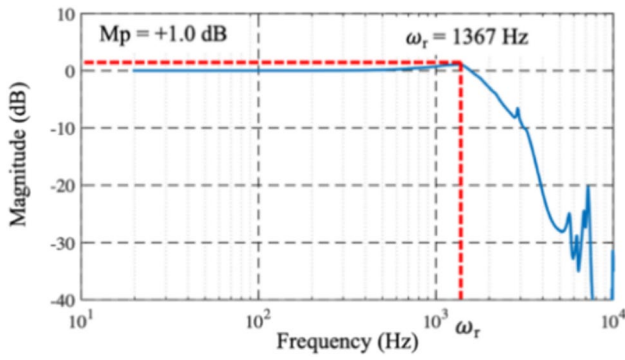


Fig. 13 Frequency response plot of the FTS system

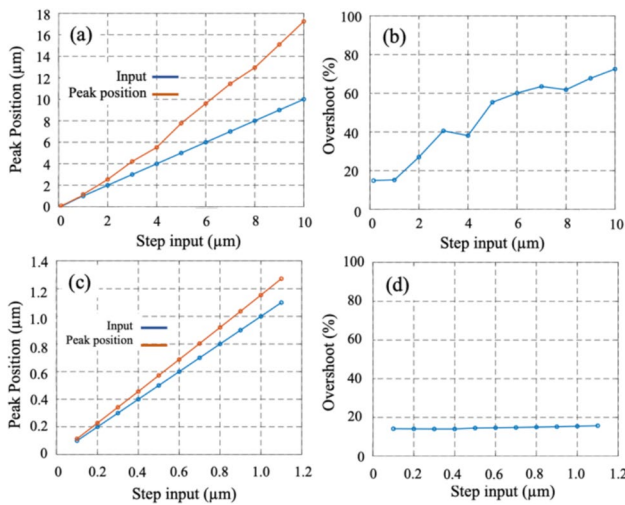


Fig. 14 a Peak position versus step input for larger inputs, b overshoot amount versus step input for larger inputs, c peak position versus step input for smaller inputs, and d overshoot amount versus step input for smaller inputs

system dynamics behavior and the waviness appearance, the machining parameters were optimized. First, the given transfer function plot calculated in the system was observed. This was derived from a system identification process by adding white noise into the system [28]. The obtained frequency response plot is shown in Fig. 13. From the results of the system information, the resonant frequency ω_r was 1367 Hz, and the resonant peak M_p was +1.0 dB. This resonant frequency is almost identical to the ripple cycle of 1333 Hz obtained from the position data. Therefore, this waviness was induced by the FTS dynamics recognized from this frequency response plot.

Figure 14 shows the relationship between the step response input and the actual position, including the overshoot amount. These data were taken by adding 0.1–10 μm step commands at the surface speed of 5 m/min. Figure 14a shows the relationship between the step input and the peak

position, while Fig. 14b shows the relationship between the step input and the overshoot amount. These data imply that the system is nonlinear because the overshoot amount does not increase by the same ratio as the input. Therefore, it is difficult to describe the behavior of the entire system with a second-order system transfer function.

The results of a smaller input bandwidth below the 1 μm step are shown in Fig. 14c, d. These results differed from those in Fig. 14a, b. The overshoot amount stayed between 14% and 15% in this bandwidth. Therefore, the smaller input area follows a linear system. In this case, for simplification, the second-order system can be applied to describe the system only in this range based on the frequency response plot results, as shown in Fig. 13 [29]. Using the frequency response plot, the transfer function $G(s)$ can be expressed using the following equation:

$$G(s) = \frac{\omega_n^2}{s^2 + 2\zeta\omega_n s + \omega_n^2}, \tag{2}$$

where s is the Laplace operator, $G(s)$ is the transfer function of the system, ω_n is the natural frequency, and ζ is the damping ratio. The damping ratio ζ and natural frequency ω_n of the system can be derived from the relationship between the peak magnitude of the frequency response M_p and the resonance frequency ω_r that is indicated in the transfer function plot with the following equations:

$$M_p = \frac{1}{2\zeta\sqrt{1-\zeta^2}}, \tag{3}$$

$$\omega_r = \omega_n\sqrt{1-2\zeta^2}. \tag{4}$$

Using the relationship between Eqs. (3) and (4), damping ratios of 0.523 and 0.855 were derived. Based on the position analysis results in Figs. 10 and 11, the position error signature of the system response exhibits a considerable peak. This indicates that the damping ratio should be less than $1/\sqrt{2}$, according to the control theory perspective [29]. Therefore, the damping ratio of this system can be approximated as 0.523. Using the derived ζ , the natural frequency ω_n can also be approximated as 2029 Hz. Thus, the approximated transfer function can be expressed as follows:

$$G(s) = \frac{4.12 \times 10^6}{s^2 + 2121s + 4.12 \times 10^6}. \tag{5}$$

By utilizing the approximated transfer function derived by Eq. (5), the system step response curve can be calculated. According to these calculation results, the system settling time of the step response can be derived. Figure 15 shows the step response curve from the approximated transfer function. The settling time does not depend on the input amount

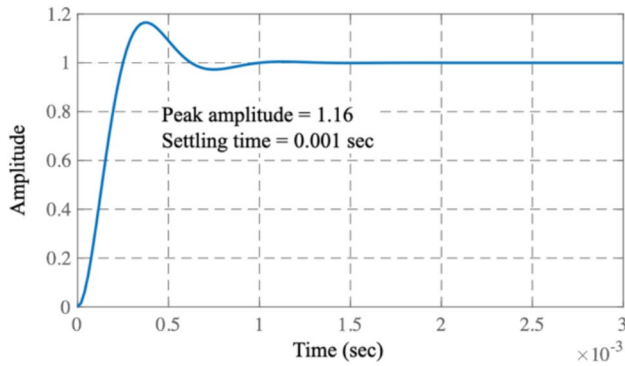


Fig. 15 Step response curve representation with second-order system simplification

because of the linear system representation. The data indicated that the settling time in this system within the linear system area had an overshoot amount of 16.4% and a settling time of 0.001 s when the determination range was set at 0.2% of the step input.

3.5 Machining Strategy for the Lens Array

As the machining strategy for fabricating the lens array shape using the FTS system, the machining conditions for the given shape shown in Table 2 were reexamined by considering the FTS system dynamics. To prevent surface waviness for uniform surface quality, the machining conditions were selected to maintain a constant surface speed based on the observed trends of waviness on the machined surface at a constant spindle speed of 125 rpm, aiming to achieve uniform servo behavior across the entire surface. Based on the results and discussion in Sect. 3.3 and Fig. 12, the theoretical settling time approximation and the actual response at a surface speed of 5 m/min were identical for the tool trajectory of the lens array design. Therefore, a surface speed of 5 m/min falls within the linear system range, and the surface speed was selected as the optimized cutting parameter in this study. Additionally, the maximum spindle speed was set to 1000 rpm to prevent exceeding the machine’s limitations, for all lenslets were covered in a constant surface speed range.

Subsequently, the approximate settling time was calculated using the derived system transfer function. Based on this settling time, a strategy was proposed to offset the tool position from the machined surface until stabilization. The offset distance from the surface was determined based on the settling time and was incorporated as part of the machining strategy.

Figure 16 illustrates the schematic of the tool trajectory along the meridian of the lenslet, taking the settling time into account. The tool trajectory of the radius area expands by

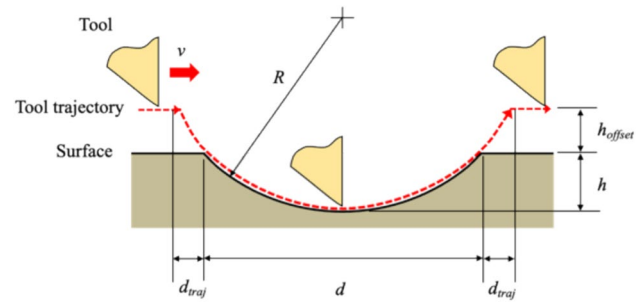


Fig. 16 Illustration of the tool trajectory at the meridian of the lenslet considering the servo settling time

twice the amount of d_{traj} to be positioned above the flat zone by an offset amount h_{offset} , calculated using Eqs. (6) and (7) based on the geometric relationships described in Fig. 14.

$$h_{offset} = \sqrt{R^2 - \left(\frac{d}{2}\right)^2} - \sqrt{R^2 - \left\{\frac{d}{2} + d_{traj}\right\}^2}, \quad (6)$$

$$d_{traj} = v \cdot T_s, \quad (7)$$

where R is the lenslet radius, d is the diameter of the lenslet, v represents the relative speed between the tool and the surface, and T_s is the settling time derived from the system transfer function. Based on the discussion in Sect. 3.3, this FTS system has a settling time of at least 0.001 s based on the step response result. Therefore, the offset amount that is required to prevent waviness can be derived from the surface speed for machining.

For a surface speed of 5 m/min applied to a 20 mm radius dimple with a 1.7 mm diameter, the offset amount was determined to be 3.7 μm from the surface, considering the minimum settling time of 0.001 s in this study. Table 4 summarizes the machining conditions designed with consideration of the dynamic behavior of the FTS system. Based on position data analysis and settling time considerations, the cutting

Table 4 Cutting conditions after optimization

Item	Value
Tool	Natural diamond tool
Tool radius (mm)	0.496
Tool rake angle ($^\circ$)	0
Tool clearance angle ($^\circ$)	13
Surface speed (m/min)	5
Spindle rotation direction	Clockwise
Finish feed rate (mm/rev)	0.002
Finish depth of the cut (mm)	0.002
Coolant	Oil mist
Offset from the surface (μm)	5.0

parameters for the demonstration were set to a surface speed of 5 m/min with a 5 μm offset from the surface in the uncut zone, ensuring sufficient settling time to prevent waviness.

Figure 17 shows a comparison of the surface waviness evaluation results before and after using the proposed machining strategy. By applying the optimized machining conditions, the average Sdq value of the 10×10 lens array improved from 93.3 to 49.9 μrad , and the standard deviation reduced from 33.5 to 3.1 μrad .

In addition, in terms of the repeatability of this machining strategy, the machining test with the cutting conditions shown in Table 5 was conducted three times. The result of the standard deviation of the average Sdq was 0.75 μrad . Therefore, the reproducibility of the surface topography was verified with repeatable results in this study.

The results related to the surface roughness after machining are shown in Fig. 18, where (a), (b), and (c) show the constant spindle speed cutting results, while (d), (e), and (f) show the results of the optimized parameter. The average Sq value and standard deviation of all lenslets before applying the proposed strategy were 2.8 and 0.78 nm, respectively, whereas those after applying the proposed strategy were 1.6 and 0.28 nm, respectively. The proposed machining strategy considerably contributed to the reduction in the variation of the surface quality.

In fabricating lens arrays using the FTS system, it is essential to use machining conditions optimized based on the dynamic behavior of the servo system. In particular, in terms of reducing waviness on the machined surface, maintaining a constant surface speed is an effective method for achieving a uniform machined surface with low surface roughness.

4 Conclusions

A 10×10 lens array was machined using an FTS-based diamond turning system, and dynamics-induced surface waviness formation was investigated. The conclusions are as follows.

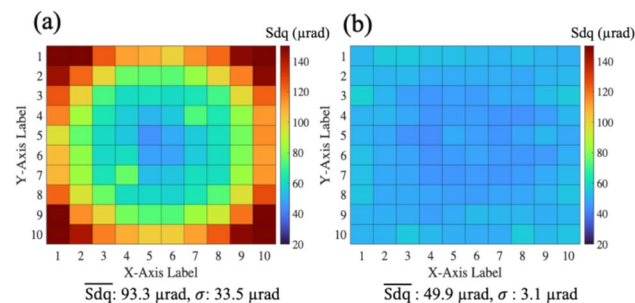


Fig. 17 Comparison of the waviness analysis results **a** at a constant spindle speed and **b** after applying the optimized cutting conditions

Table 5 Reproducibility results of the machining tests using the proposed strategy

Sample number	$\overline{\text{Sdq}}(\mu\text{rad})$
#1	49.9
#2	48.4
#3	49.0
Average	49.1
Standard deviation	0.75

1. At a constant spindle speed, the machined surface exhibited considerable waviness at the corner lenslet. The waviness amount was high outside the lenslet. The waviness amount was quantified using the parameter Sdq.
2. The position signal analysis results showed a similar waviness pattern on the surface, indicating that the pattern originated from the servo response.
3. The control system characteristics were derived by analyzing the input and output signals using the frequency response plot and step response curve. This system had a resonant frequency of 1367 Hz and a settling time of 0.001 s within the bandwidth, representing a linear system.
4. The cutting parameters were optimized based on the relationship between settling time consideration and analysis of the dynamics-induced surface waviness formation. As a result, the surface waviness is greatly reduced.
5. An average Sdq value of 49.9 μrad and a standard deviation of 3.1 μrad were achieved using the proposed strategy, indicating a 53% reduction in the average waviness amount and a 90% reduction in the standard deviation.

This study contributes to the ultraprecision manufacturing of lens arrays, freeform optics, and other structured surfaces using an FTS system. By optimizing the cutting parameters based on the proposed machining strategy, the form accuracy

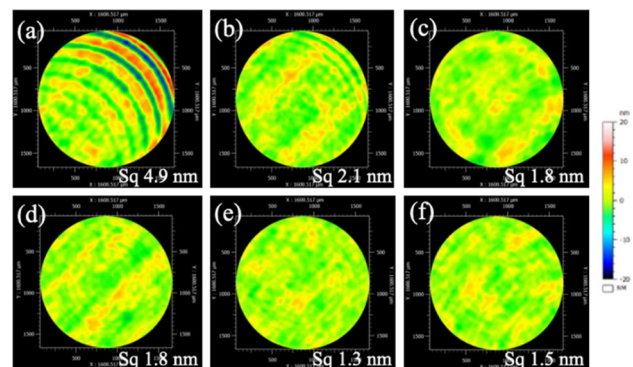


Fig. 18 Surface roughness comparison for various spindle speeds and lenslet locations: **a** 125 rpm, (1,1), **b** 125 rpm, (3,3), **c** 125 rpm, (5,5), **d** optimized, (1,1), **e** optimized, (3,3), and **f** optimized, (5,5)

and surface roughness of optical components can be considerably improved.

Acknowledgements The authors would like to extend thanks to AME-TEK Precitech Inc., USA, and Zygo Corporation, USA, for providing technical support and information on the ultraprecision diamond turning machine and the fast tool servo system used in this study.

Authors' contributions Takeshi Hashimoto: Writing – original draft, Visualization, Methodology, Investigation, Formal analysis, Data curation, Conceptualization. Jiwang Yan: Supervision, Resources, Project administration, Methodology, Funding acquisition, Conceptualization, Writing - review & editing. All authors read and approved the final manuscript.

Availability of Data and Materials No data are associated with the manuscript.

Declarations

Competing interests Jiwang Yan is an editorial board member for "Nanomanufacturing and Metrology" and was not involved in the editorial review, or the decision to publish this article. The authors declare that they have no known competing financial interests or personal relationships that could have appeared to influence the work reported in this paper.

Open Access This article is licensed under a Creative Commons Attribution 4.0 International License, which permits use, sharing, adaptation, distribution and reproduction in any medium or format, as long as you give appropriate credit to the original author(s) and the source, provide a link to the Creative Commons licence, and indicate if changes were made. The images or other third party material in this article are included in the article's Creative Commons licence, unless indicated otherwise in a credit line to the material. If material is not included in the article's Creative Commons licence and your intended use is not permitted by statutory regulation or exceeds the permitted use, you will need to obtain permission directly from the copyright holder. To view a copy of this licence, visit <http://creativecommons.org/licenses/by/4.0/>.

References

- Hung K-Y, Hsiao P-J, Tseng F-G, Wei M-C (2011) From spheric to aspheric solid polymer lenses: a review. *Adv Optoelectron* 2011:197549. <https://doi.org/10.1155/2011/197549>
- Vishweshwar Rao B, Kiran M, Venkateswaran R, Sriram KV, Narayanamurthy CS (2023) Convex optical freeforms using fringe Zernike overlay approach for two-mirror and three-mirror telescopes for space applications. *Opt Commun* 541:129533. <https://doi.org/10.1016/j.optcom.2023.129533>
- Essilor (2023) Stellest lenses: a game-changing innovation in myopia control for children. <https://www.essilor.com/uk-en/products/stellest/>
- Huang Y, Li X, Zhuo Z, Zhang J, Que T, Yang A, Drobe B, Chen H, Bao J (2024) Effect of spectacle lenses with aspherical lenslets on choroidal thickness in myopic children: a 3-year follow-up study. *Eye Vis* 11:16. <https://doi.org/10.1186/s40662-024-00383-4>
- Maimone A, Wang J (2020) Holographic optics for thin and light-weight virtual reality. *ACM Trans Graph* 39:67. <https://doi.org/10.1145/3386569.3392416>
- Kress BC, Pace M (2022) Holographic optics in planar optical systems for next generation small form factor mixed reality headsets. *Light Adv Manuf* 3:42. <https://doi.org/10.37188/lam.2022.042>
- Li L, Yi AY (2010) Development of a 3D artificial compound eye. *Opt Express* 18:18125–18137. <https://doi.org/10.1364/OE.18.018125>
- Liu J, Lombardo S, Muslimov E, Chebbo M, Hugot E (2022) Innovative optical design combining freeform optics and curved-freeform sensors. *Proc SPIE* 12188:121882O. <https://doi.org/10.1117/12.2629193>
- Platt BC, Shack R (2001) History and principles of Shack-Hartmann wavefront sensing. *J Refract Surg* 17:S573–S577. <https://doi.org/10.3928/1081597X-20010901-05>
- Lukin VP, Botygina NN, Emaleev ON, Korolkov VP, Lavrinova LN, Nasyrov RK, Poleshchuk AG, Cherkashin VV (2009) Shack-Hartmann sensor based on a low-aperture off-axis diffraction lens array. *Optoelectron Instrum Data Process* 45:161–170. <https://doi.org/10.3103/S8756699009020101>
- Schwarz S, Götzendorfer B, Rung S, Esen C, Hellmann R (2021) Compact beam homogenizer module with laser-fabricated lens-arrays. *Appl Sci* 11(3):1018. <https://doi.org/10.3390/app11031018>
- Wippermann F, Zeitner UD, Dannberg P, Bräuer A, Sinzinger S (2007) Beam homogenizers based on chirped microlens arrays. *Opt Express* 15(10):6218–6229. <https://doi.org/10.1364/OE.15.006218>
- Bao J, Yang A, Huang Y, Li X, Pan Y, Ding C, Lim EW, Zheng J, Spiegel DP, Drobe B, Lu F, Chen H (2022) One-year myopia control efficacy of spectacle lenses with aspherical lenslets. *Br J Ophthalmol* 106:1171–1176. <https://doi.org/10.1136/bjophthalmol-2020-318367>
- Gantes-Nuñez J, Jaskulski M, López-Gil N, Kollbaum PS (2023) Optical characterisation of two novel myopia control spectacle lenses. *Ophthalmic Physiol Opt* 43:388–401. <https://doi.org/10.1111/opo.13098>
- Brinksmeier E, Gläbe R, Schönemann L (2012) Review on diamond-machining processes for the generation of functional surface structures. *CIRP J Manuf Sci Technol* 5:1–7. <https://doi.org/10.1016/j.cirpj.2011.10.003>
- Zhang P, Du Y, Wang B, Shan D (2014) Fabrication of micro-lens array on convex surface by means of micro-milling. *Proc SPIE* 9281:928106. <https://doi.org/10.1117/12.2069855>
- Brinksmeier E, Karpuschewski B, Yan J, Schönemann L (2020) Manufacturing of multiscale structured surfaces. *CIRP Ann Manuf Technol* 69:717–739. <https://doi.org/10.1016/j.cirp.2020.06.001>
- Wang Z, Chen Z, Zhang X (2022) Profile compensation for single-point diamond turning of microlens array. *Nanomanuf Metrol* 5:403–411. <https://doi.org/10.1007/s41871-022-00147-5>
- Yuan W, Li L-H, Lee W-B, Chan C-Y (2018) Fabrication of microlens array and its application: a review. *Chinese J Mech Eng* 31(1):16. <https://doi.org/10.1186/s10033-018-0204-y>
- Liu Y-T (2024) Recent development of piezoelectric fast tool servo (FTS) for precision machining. *Int J Precis Eng Manuf* 25:851–874. <https://doi.org/10.1007/s12541-023-00913-5>
- To S, Kwok TC, Cheung CF, Lee WB (2006) Study of ultra-precision diamond turning of a microlens array with a fast tool servo system. In: *Proceedings of SPIE—The international society*

- for optical engineering, vol 6149, p 61490S. <https://doi.org/10.1117/12.674215>
22. Tanikawa S, Yan J (2022) Fabrication of micro-structured surface with controllable randomness by using FTS-based diamond turning. *Precis Eng* 73:363–376. <https://doi.org/10.1016/j.precisioneng.2021.10.005>
 23. Huang P, To S, Zhu L, Tang Y, Zhu Y (2020) Deterioration of form accuracy induced by servo dynamics errors and real-time compensation for slow tool servo diamond turning of complex-shaped optics. *Int J Mach Tools Manuf* 154:103556. <https://doi.org/10.1016/j.ijmachtools.2020.103556>
 24. Zhang L, Sato Y, Yan J (2023) Optimization of fast tool servo diamond turning for enhancing geometrical accuracy and surface quality of freeform optics. *J Adv Mech Des Syst Manuf* 17:JAMDSM0012. <https://doi.org/10.1299/jamdsm.2023jamdsm0012>
 25. Filip J, Vávra R, Maile FJ (2023) Waviness analysis of glossy surfaces based on deformation of a light source reflection. *J Coat Technol Res* 20:1703–1712. <https://doi.org/10.1007/s11998-023-00775-6>
 26. AMETEK Precitech Inc (2024) FTS5000 specification <https://www.precitech.com/product/accessoriesoverview/fasttoolservo>.
 27. International Organization for Standardization (2021) Geometrical product specifications (GPS)—Surface texture: Areal—Part 2: Terms, definitions and surface texture parameters (ISO Standard No. 25178-2:2021).
 28. Ljung L (1999) *System identification: theory for the user*, 2nd edn. Prentice Hall PTR, Upper Saddle River
 29. Nise NS (2019) *Control systems engineering*, 8th edn. Wiley, Hoboken, pp 168–208

Publisher's Note Springer Nature remains neutral with regard to jurisdictional claims in published maps and institutional affiliations.



Takeshi Hashimoto is currently a Ph.D. student in integrated design engineering at Keio University under the supervision of Prof. Jiwang Yan. His research interests include ultraprecision diamond turning of optics surfaces, machine tool design and control systems for ultraprecision machines. He also works for AMETEK Precitech Inc. as an application engineer.



Jiwang Yan received his Ph.D. from Tohoku University, Japan in 2000 and is currently a professor of Mechanical Engineering at Keio University (2012–now), leading the Laboratory for Precision Machining and Nano Processing. His research areas include ultraprecision machining, micro/nano manufacturing, laser processing, nanomaterials, and nanomechanics.